Effect of multilayering and crystal orientation on spin-orbit torque efficiency in Ni/Pt layer stacking

A. Sud,[1,2,*] Y.-C. Lau,[3,4] J. Brierley,[2,5,6] H. Kurebayashi,[2,5,1] and T. Seki[3,†]

[1]*WPI-AIMR, Tohoku University, 2-1-1, Katahira, Sendai 980-8577, Japan*

[2]*London Centre for Nanotechnology, University College London, 17-19 Gordon Street, London, WC1H 0AH, United Kingdom*

[3]*Institute for Materials Research, Tohoku University, 2-1-1, Katahira, Sendai 980-8577, Japan*

[4]*Institute of Physics, Chinese Academy of Sciences, Beijing 100190, China*

[5]*Department of Electronic & Electrical Engineering, University College London, 7JE, Malet Pl., London WC1E 7JE, United Kingdom*

[6]*ISIS Neutron and Muon Source, Rutherford Appleton Laboratory, Harwell Oxford, Didcot OX11 0QX, United Kingdom*

(Received 6 March 2023; revised 9 September 2023; accepted 7 December 2023; published 20 December 2023)

We study spin-orbit torques (SOTs) in Ni/Pt bilayers and multilayers by ferromagnetic resonance (FMR) and harmonic-Hall measurements. The effect of multilayering and crystal orientation on fieldlike (FL) and dampinglike (DL) torque efficiencies is examined by exploiting the samples with different crystal orientations: epitaxial and polycrystalline structures on sapphire and SiO_2 substrates, respectively. We find that both DL and FL torque efficiencies are larger in multilayer samples and there is no complete cancellation of torque efficiencies that is generally expected for ideal symmetric stacking structures. The results of SOT-FMR indicate that the epitaxial samples show higher efficiency for SOT generation compared to the polycrystalline samples, suggesting that SOT generation is modified depending on the interfacial contribution. In addition, the spin Hall conductivity of the epitaxial multilayer is the largest among the samples. The present results signify the importance of crystal orientation, multilayering, and interface quality in improving the efficiency of SOT generation combined with larger spin Hall angle for developing future spintronic devices.

DOI: 10.1103/PhysRevMaterials.7.124410

I. INTRODUCTION

Spin-orbit torques (SOTs) [1–8] provide an efficient way to manipulate the magnetization in ferromagnetic single layers or heterostructures with large spin-orbit coupling. Two mechanisms responsible for the SOTs in ferromagnetic/heavy-metal (FM/HM) bilayers are based on the creation of nonequilibrium spin polarization by electric current [2]. The first mechanism is attributed to the spin Hall effect (SHE) [9–11], which occurs in a nonmagnetic layer that converts a charge current into a transverse spin current. The generated spin current then diffuses to the ferromagnetic layer through spin angular momentum transfer, which exerts a torque. The second mechanism of generation of SOTs occurs at the interface due to interfacial spin-orbit coupling in the FM/HM bilayers. When the inversion symmetry is broken at the interface, the spin-orbit Hamiltonian lifts the degeneracy of electron-spin momentum states. Because of this spin-orbit term, a charge current flowing parallel to the interface is to be spin polarized. This process is called the Rashba-Edelstein effect (inverse spin galvanic effect) [12–14]. The resultant spin polarization can exert torques in the adjacent FM layer [15]. Both mechanisms can result in dampinglike (DL) torque $\sim\tau_{\mathrm{DL}}(\mathbf{m}\times(\sigma\times\mathbf{m}))$ and fieldlike (FL) torque $\sim\tau_{\mathrm{FL}}(\sigma\times\mathbf{m})$ [16]. Here, $\mathbf{m}$ is the unit vector of magnetization, σ is the spin polarization in the direction of the spin current, and $\tau_{\mathrm{DL(FL)}}$ is the magnitude of torque which has already been described in detail in previous works [17–19]. In real systems, it might be intuitively appealing to track down and parse the resultant torque into these two contributions. However, the SOT scenario is often complicated due to the presence of local spin currents [20] within the ferromagnet, which can also contribute to torque generation. Moreover, in thin films the existence of orbital effects can produce unconventional torques [21]. Understanding the interplay between bulk, interfacial, and orbital contributions to SOT is important to enhance the efficiency of SOT devices.

The SOT efficiency is a figure of merit for characterizing its potential for future spintronic applications. Materials which can offer higher SOT efficiency are continuously being investigated, including ferromagnets, antiferromagnets [22], two-dimensional materials [23], heavy metals [24], and topological insulators [25]. The quest for efficient sources for SOT generation raises many questions about the mechanism and the magnitude of their effectiveness in SOT enhancement. What is the nature of spin orbit effects that can lead to larger SOTs? Is there any significant variation in torque efficiency dependent on multilayer composition, thickness, or interface modification? A number of such open questions remain that can have an impact on future developments. A proper interpretation of torque efficiency is highly complex, owing to its

*aakanksha.sud.c1@tohoku.ac.jp
†takeshi.seki@tohoku.ac.jp

TABLE I. Summary of the sample notation used, stacking pattern, deposition temperature, and substrate used. The RHEED and XRD confirm the epitaxial/polycrystalline growth. The numbers in brackets represent thicknesses in nm. The easy axes of magnetization are also presented.

Sample	Substrate	Deposition temperature	Stack	RHEED, XRD	Easy axis
K-01	sapphire	400 °C	$[Pt(1)/Ni(3)]_{\times 5}\vert Al_2O_3(5)$	(111) epitaxial	in plane
K-02	SiO_2	Room temperature	$[Pt(1)/Ni(3)]_{\times 5}\vert Al_2O_3(5)$	polycrystalline	in plane
K-03	sapphire	400 °C	$[Pt(1)/Ni(3)]\vert Al_2O_3(5)$	(111) epitaxial	in plane
K-04	SiO_2	Room temperature	$[Pt(1)/Ni(3)]\vert Al_2O_3(5)$	polycrystalline	in plane

origin in both bulk as well as interfacial effects [26]. The interface quality as well as film structure can have prolific influence on the torque efficiency [27–29], shedding light on the importance of sample growth conditions that significantly influence the SOT efficiency [30–32]. Moreover, spin relaxation mechanisms are dependent on crystal morphology and structure, which can influence SOTs [33,34]. Both Elliot-Yafet (EY) [35,36] and Dyakanov-Perel (DP) relaxation [33] mechanisms can be modulated by structural changes [37]. Additionally, enhanced SOT efficiencies have been reported in multilayers with ferromagnet sandwiched between two nonmagnets having opposite spin Hall angles [38]. The presence of planar Hall effect causes additional antidamping torque in asymmetric structures. These facts reported by previous studies imply that the crystal structure [39–41] as well as the interfacial effects play a role in SOT generation and modification.

In this paper, we study the effect of multilayering and crystal orientation on the generation of SOTs in Ni/Pt bilayers and multilayers. This is done using ferromagnetic resonance (FMR) and harmonic-Hall measurements. There have been some interesting results on SOT engineering in multilayer systems, for example, in Co/Pt multilayers [42–44] and some other works demonstrating the role played by interfaces in the origin of unconventional SOT behaviors in multilayer stacks of Co/Pd [45]. These works suggest that multilayers will provide a research stage different from the bilayer cases. Apart from several works in Co-based multilayers, there has been only one work investigating SOT in Ni/Pt bilayer systems [26]. However, they do not report the case of multilayer. Both Co and Ni have face-centred cubic lattices, but very different electronic structures giving rise to totally different magnetic and transport properties. This means that Ni/Pt is a candidate system for the extensive study on the potential of multilayer as a SOT material. Since epitaxial growth is also possible for the Ni/Pt multilayers, Ni/Pt is considered to be a suitable material to investigate the influence of film crystallinity on the magnitude of SOT. This should provide promising directions towards the development of SOT in other thin-film stacks. The samples used for this study were grown on sapphire and SiO_2 substrates, which show epitaxial and polycrystalline growth as revealed by our structural analysis. We found DL torque efficiency, from FMR measurements, shows a large enhancement in multilayer epitaxial samples, which is about 160% larger than bilayer polycrystalline samples. The values for DL torque efficiency are in agreement with those obtained from harmonic-Hall measurements. The multilayer epitaxial samples also exhibit the largest FL torque efficiencies. Furthermore, the results of FMR linewidth modulation confirm a larger spin Hall angle ∼0.15 in these samples. Our results demonstrate the importance of growth on SOT efficiency and also its effect on various magnetic parameters. We illustrate an efficient approach to improve the SOT efficiency, which is achieved by growing multilayer epitaxial samples.

II. SAMPLE GROWTH, CHARACTERIZATION AND DEVICE FABRICATION

A. Film growth

The Ni/Pt multilayer films were grown using magnetron sputtering in an ultrahigh vacuum system with a base pressure below 2×10^{-7} Pa. Two types of substrates were used: sapphire(0001) and SiO_2 for epitaxial and polycrystalline growth, respectively. A Pt layer was first deposited on top of the substrate followed by growth of the Ni layer. The thicknesses of the Ni and Pt layers were fixed at 3 and 1 nm, respectively, for all the samples. The sample label and stack structure is summarized in Table I, where $[Ni/Pt]_{\times 5}$ represents the five time repetition of [Ni/Pt] layers.

The deposition temperature was optimized to achieve the epitaxial growth on sapphire and to ensure successful formation of the layered structure [46]. These conditions were met at a temperature of 400 °C, which was maintained constant throughout the deposition process. Finally, a 5-nm-thick Al_2O_3 capping layer was deposited on the top. The magnetic anisotropy induced at the interface of Ni/Al_2O_3 was negligible, confirmed by using a reference sample of Ni single-layer film with Al_2O_3 capping layer. The samples K-02 and K-04 were deposited on SiO_2 substrate at room temperature.

B. Film characterization

The crystal orientation and morphology were monitored *in situ* during growth using reflection high-energy electron diffraction (RHEED) and we present some of them in Fig. 1. Polycrystalline growth is confirmed by the presence of rings for the sample grown on a SiO_2 substrate [Figs. 1(c) and 1(d)] while sharp periodic streaks correspond to epitaxial growth on a sapphire substrate [Figs. 1(a) and 1(b)]. Structural characterization was performed using x-ray diffraction (XRD) techniques with Cu-$K\alpha$ radiation shown in Fig. 2 for K-01 and K-02. The diffraction profile calculated by the Laue function with the assumption of the step model for the superstructure is also displayed on top of the XRD profiles. For this model, $[Ni\ (3\ nm)\ /Pt\ (1\ nm)\ ]_{\times 5}$ with the (111) crystal orientation was assumed (See Appendix for more details). The XRD profile of K-01 shows a clear multiple-peak structure, whose peak positions are explained by the calculated XRD profiles,

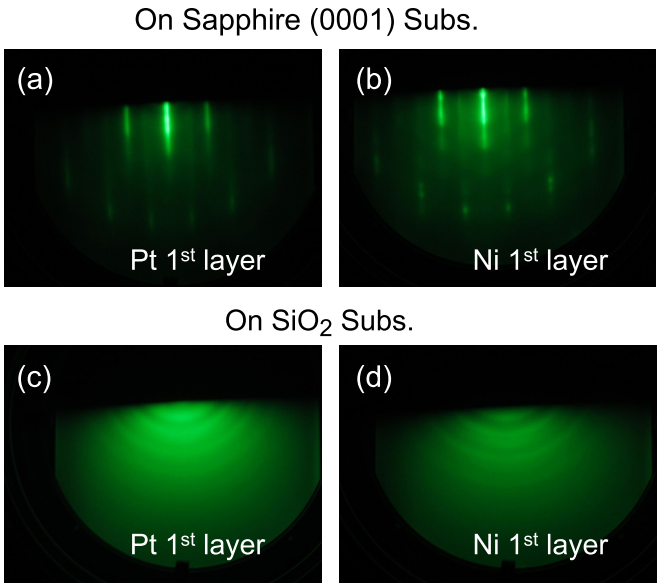

FIG. 1. Reflection high-energy electron diffraction patterns for samples K-01 and K-02 grown on sapphire and SiO_2, respectively. The diffraction patterns were observed just after the growth of the first Ni and Pt layers.

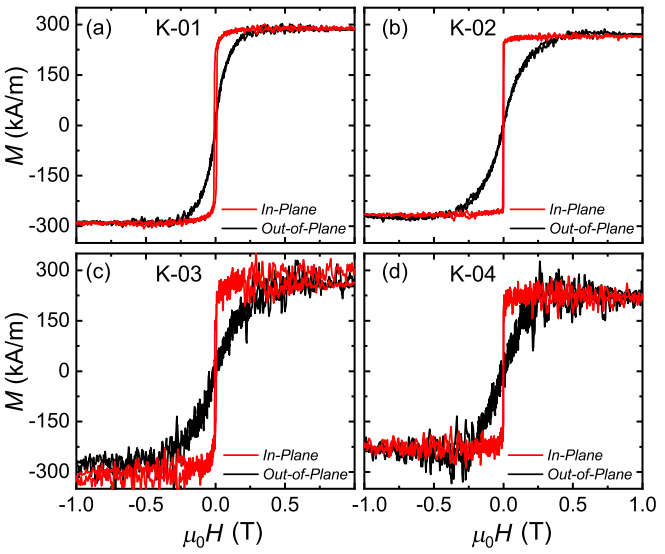

FIG. 3. Magnetization curves for the samples measured using vibrating sample magnetometer (VSM). The red curves are the results measured with in-plane magnetic field (IP) while the black curves denote the measurements with out-of-plane magnetic field (OOP). The measurements were done at room temperature.

indicating that the K-01 film is a well-defined superlattice with the designed thicknesses and the (111) crystal orientation. In contrast to K-01, sample K-02 exhibits a few small peaks around $2\theta = 40^\circ$. Taking into account the fact that the RHEED patterns are the ring shapes for K-02, we confirm that K-02 is a polycrystalline film. However, its XRD peak positions fairly match with those calculated. This suggests that the (111) crystal orientation is preferential in the film, despite its polycrystalline behavior confirmed by RHEED. An important point is that the calculated XRD profile uses the bulk lattice constant of Ni and Pt, and the calculation results can explain the peak positions of both K-01 and K-02, suggesting that there is no remarkable difference in the lattice constant between K-01 and K-02. Thus, from both RHEED and XRD results, it is confirmed that the samples grown on sapphire substrates show epitaxial growth whereas those on SiO_2 form a polycrystalline film.

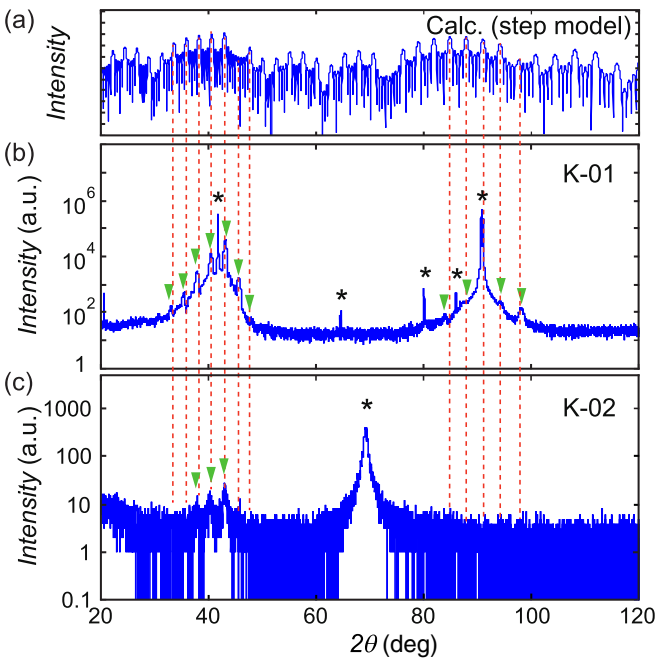

FIG. 2. X-ray diffraction profiles of (a) calculation, (b) K-01 sample grown at 400 °C on sapphire substrate and (c) K-02 sample grown at room temperature on SiO_2 substrate. The black asterisks denote the diffractions from the substrates and the green inverted triangles denote the diffractions of multilayered structures. The calculation was done using the Laue function with the assumption of the step model for the superstructure. The red dotted lines are guides indicating the peak positions for the superlattice with the (111) crystal orientation.

The magnetic hysteresis loops were measured using a vibrating sample magnetometer at room temperature. Figure 3 shows the magnetization curves for the four samples obtained when applying field $\mu_0 H$ along in-plane (red curves) and out-of-plane directions (black curves) of the films. All the samples are in-plane favored materials with coercivity of approximately 10 mT. Table II summarizes the estimated saturation magnetization values ($\mu_0 M_s$) for the different samples.

TABLE II. Efficiency magnitude for dampinglike (ξ_{DL}) and fieldlike (ξ_{FL}) torques per applied current density j, spin Hall conductivity (σ_{SH}), and the saturation magnetization ($\mu_0 M_S$) of the samples.

	Sample			
Parameter	K-01	K-02	K-03	K-04
ξ_{DL}	0.08	0.06	0.04	0.03
ξ_{FL}	0.04	0.02	0.003	0.0004
$\sigma_{SH}((\hbar/2e)10^3\Omega^{-1}\text{cm}^{-1})$	7.0	4.6	2.2	1.0
$\mu_0 M_s(T)$	0.362	0.331	0.377	0.298

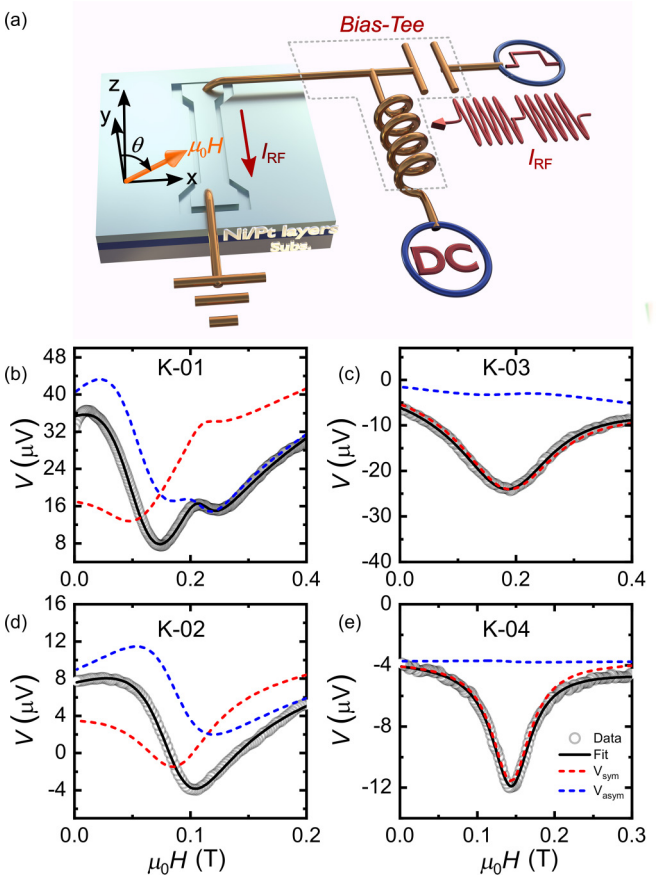

FIG. 4. Schematic illustration of the experimental setup used for SOT-FMR experiments. The microwave current, I_{RF} is injected into the bar with width 5 μm through a bias-tee. θ denotes the in-plane angle between the external field $\mu_0 H$ and the microstrip. (b)–(d) Magnetic field dependence of the dc voltage, V, for the samples measured at 8 GHz. The data points are fitted (solid black line) with a combination of symmetric (dashed red line) and antisymmetric (dashed blue line). A clear antisymmetric component is visible for multilayer sample as compared to bilayer sample (K-03, K-04).

C. Device fabrication

To study the spin transport by SOT-FMR measurements, the samples were cut into 5 mm × 5 mm chips prior to device fabrication using standard lithography and Ar-ion milling techniques. Rectangular bars of width 5 μm and length of 400 μm (K-01 and K-02) and 200 μm (K-03 and K-04) were defined for FMR measurements. The device circuitry and bar pattern are illustrated in Fig. 4(a). For harmonic-Hall resistance measurements, the samples were patterned in the form of symmetric Hall cross structures as shown in the inset of Fig. 9(a). The length and width of the Hall bar were 25 μm and 10 μm. respectively.

III. MEASUREMENT TECHNIQUES

We quantified the SOT efficiency and magnetic parameters using two independent techniques of SOT-FMR and harmonic-Hall resistance measurements as described below.

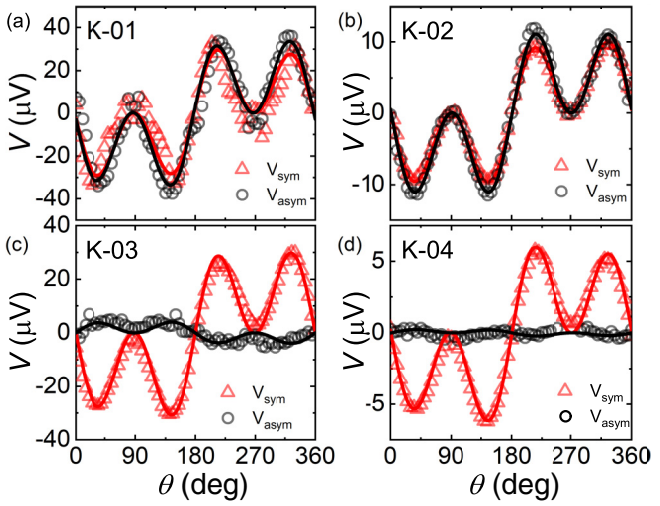

FIG. 5. The symmetric and antisymmetric components of the SOT-FMR spectra as a function of in-plane magnetic field angle θ for (a) K-01, (b) K-02, (c) K-03, and (d) K-04 films at $f = 8$ GHz. The bilayer samples show negligible antisymmetric component while the antisymmetric component is comparable to symmetric component for the multilayer samples.

A. Spin-orbit torque ferromagnetic resonance

By FMR measurements, we were able to extract the SOT efficiency in Ni/Pt multilayer films. The measurement setup is illustrated in Fig. 4(a). Microwaves at a fixed frequency, f, were injected into the bar while sweeping the external dc magnetic field at different angles, θ, from the bar direction. The effective magnetic fields (h_x, h_y, h_z) were generated from an injected microwave current, which then exerts SOT on the adjacent FM layer into precession. This magnetization precession causes a time varying change in sample resistance due to anisotropic magnetoresistance (AMR) and produces a dc voltage, V, due to rectification [4]. Figures 4(b)–4(e) show a typical voltage signal for different samples measured at $f =$ 8 GHz and $\theta = 45^\circ$ together with the fitted curves obtained using the sum of symmetric and antisymmetric Lorentzian given by Eq. (D1) (see Appendix D for details).

The DL and FL SOT efficiencies are calculated using the value of effective fields obtained by fitting the angular dependence of symmetric and antisymmetric components of V (see Appendix D). The symmetric component of voltage, $V_{sym} \propto h_z$, is related to DL torques, whereas the FL torques and Oersted torques are obtained from the antisymmetric component, $V_{asym} \propto h_x$, h_y. In Fig. 5, we plot the V_{sym} and V_{asym} obtained at different θ for all samples. The black (red) solid lines shown in Fig. 5 are obtained using Eq. (D3) (D2), from which we extract the values of h_x, h_y (h_z) summarized in Table VI. We allowed h_z in Eq. (D2) to be angular dependent as $h_z = a + b\cos\theta + c\sin\theta$. The field values are summarized in Table VI in the Appendix. h_y and b are dominant in FL and DL torques, respectively, consistent with the standard Oersted FL and spin-Hall DL pictures. From these values, we obtain the combined FL spin-orbit and Oersted effective field (H_{FL+Oe}) and DL spin-orbit effective field (H_{DL}), respectively. It can be seen from Fig. 5 that bilayer films have a very weak value of V_{asym} component. Interestingly, the sign of V_{sym} is

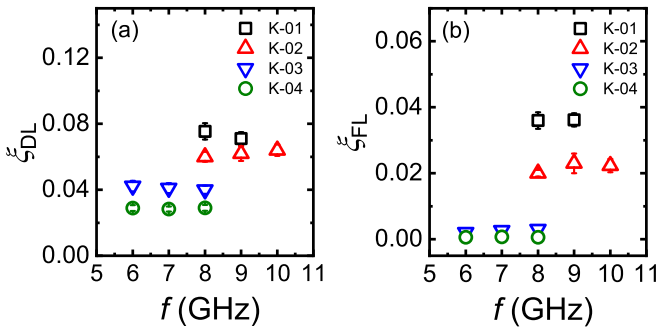

FIG. 6. Efficiency for dampinglike (ξ_{DL}) and fieldlike (ξ_{FL}) torques per applied current density j calculated using Eq. (1) at different frequencies.

constant in all samples whereas the sign of V_{asym} flips in the bilayer films. This suggests the presence of an additional FL torque term other than the Oersted origin, which seems to be thickness and material parameter dependent [47] in our bilayers.

Using the value of H_{DL}(H_{FL+Oe}), we estimated the DL (FL) efficiency per unit applied current density as

$$\xi_{DL(FL+Oe)} = \left(\frac{2e}{\hbar}\right)\frac{\mu_0 M_s d_{FM} H_{DL(FL+Oe)}}{j}, \quad (1)$$

where d_{FM} and j are the thickness of Ni and the applied current density, respectively. The values of ξ_{DL} and ξ_{FL} are summarized in Table II. It is found that the values of ξ_{DL} and ξ_{FL} are largest for the multilayer and epitaxial films. For both multilayer and bilayer films, the SOT efficiency is larger when grown epitaxially on the sapphire substrate. Experimental results at different frequencies (see Figs. 6 and 14) support reproducibility of ξ_{DL} and ξ_{FL}.

To characterize the SOT efficiency, the FMR linewidth $\mu_0\Delta H$ was measured as a function of dc current, similar to the technique used in Ref. [1], and the results are shown in Fig. 7. A clear linewidth broadening is observed for both $\theta = 45^\circ$ and $\theta = 225^\circ$. The macrospin model can provide the linewidth

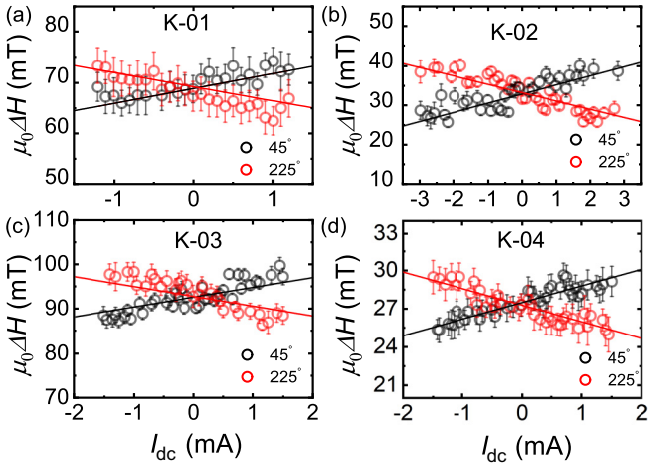

FIG. 7. The change of the FMR linewidth as a function of injected current I_{dc} at frequency of 8 GHz for K-01, K-02 and 6 GHz for K-03, K-04.

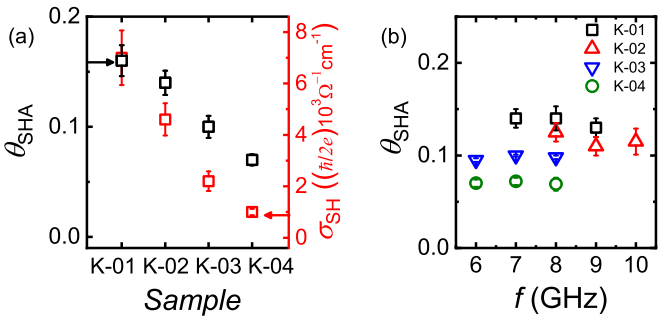

FIG. 8. θ_{SHA} calculated from (a) slope of Fig. 7 for all samples and (b) from slope of power dependence (Fig. 13) at different frequencies. The results calculated for bilayer samples are consistent for all three methods. It can be seen that epitaxial samples have larger θ_{SHA} compared to polycrystalline samples, thus indicating the role of crystal structure in modifying SOT. The right axes of (a) shows the spin Hall conductivity σ_{SH} calculated using the value of θ_{SHA}.

broadening as [1]

$$\mu_0\Delta H = \frac{2\pi f}{\gamma}\left(\alpha + \frac{\sin\theta}{(H_{ext} + 0.5M_{eff})\mu_0 M_S d_{FM}}\frac{\hbar\theta_{SHA}J_C}{2e}\right). \quad (2)$$

In Eq. (2), the terms γ, e, $\hbar$, d_{FM}, and H_{ext} are the gyromagnetic ratio, electronic charge, reduced Planck's constant, thickness of the ferromagnet, and magnetic field, respectively. Using Eq. (2), we calculated the effective spin Hall angle given as $\theta_{SHA} = J_s/J_c$, where J_s is the spin current density in the Pt layer and J_c is the charge current density. θ_{SHA} takes into account not only the contribution from bulk SHE but also other contributions originating from spin-orbit coupling as discussed in Sec. IV. θ_{SHA} for each sample is presented in Fig. 8(a). We can see a similar trend of the values of θ_{SHA} and ξ_{DL} with respect to the sample supporting our claim that multilayer and epitaxial growth enhances the SOTs.

In the multilayer samples, we still observe sizable values of θ_{SHA}. We discuss the details about this enhancement in multilayer samples in the Discussion section. We therefore use Eq. (2) to characterize averaged torques generated in the entire FM layers, from which the efffective spin-Hall angle in the entire device can still be discussed. We would like to mention here that the θ_{SHA} for multilayer epitaxial samples ~0.15 is larger than previous reported values [48–50]. This provides a route for enhancement of θ_{SHA} through growth.

To validate the conclusions drawn, we used another method for obtaining θ_{SHA}. This was done by calculating the slope of the power dependence of V_{sym} (see Appendix E and Fig. 13) using the method given in Ref. [51]. We show the calculated values of θ_{SHA} in Fig. 8(b). We obtained values similar to that obtained by linewidth modulation with current. Thus, we can confirm that multilayer epitaxial samples show large θ_{SHA}. Using the value of θ_{SHA}, we calculated the spin Hall conductivity [52] and summarized the values in Table II and Fig. 8(a). It is seen that the largest spin Hall conductivity is exhibited by epitaxial multilayer samples, which also show the largest spin Hall angle. Based on the above results, we

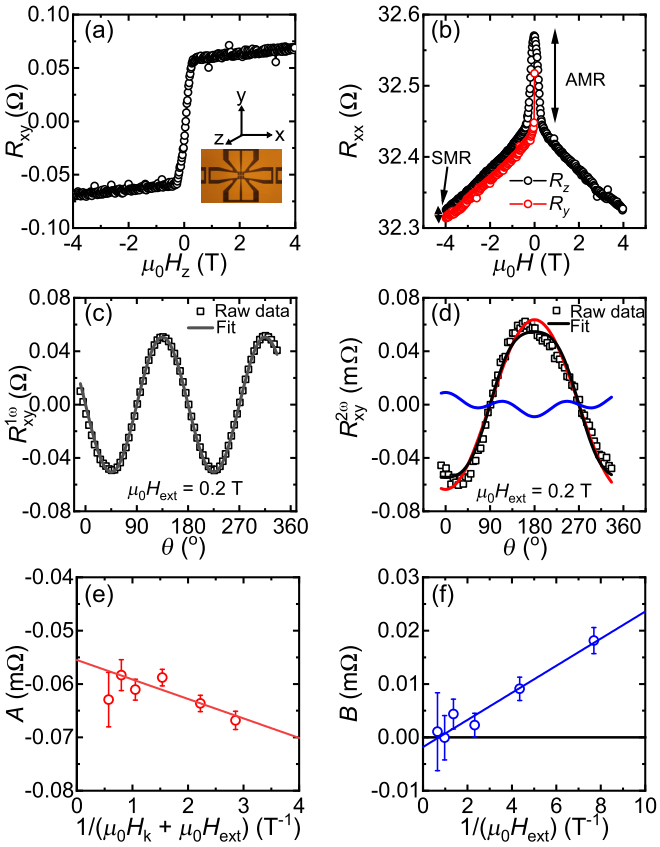

FIG. 9. (a) Transverse Hall resistance, R_{xy}, for the Hall-bar device measured with field applied along the out-of-plane direction. (b) Longitudinal resistance, R_{xx}, for the same device measured for the field applied along in-plane (red) and out-of-plane (black) directions. Angular dependence of harmonic Hall resistance at external fields of 0.2 T for (c) $R_{xy}^{1\omega}$ and (d) $R_{xy}^{2\omega}$. Black lines are the fit to the experimental data using $\sin\theta$ and Eq. (3) for (c) and (d), respectively. (d) Red and blue lines correspond to the $\cos\theta$ component (A) and $\cos 2\theta \cos\theta$ component (B), respectively. (e) Prefactor A of the $\cos\theta$ component and (f) prefactor B of the $\cos 2\theta \cos\theta$ component as a function of $1/(H_k + H_{ext})$ and $1/(H_{ext})$, respectively. Solid lines are the linear fit to the data from which the values of H_{DL} and H_{FL+Oe} are obtained.

can claim that crystal orientation effects and growth play an important role in efficient SOT generation.

B. Spin-orbit torque harmonic Hall measurements

We also calculated the SOT efficiency by measuring harmonic Hall resistance. The inset of Fig. 9(a) shows the device pattern for harmonic-Hall measurements fabricated on sample K-01. The average resistivity was found to be 26 $\mu\Omega$ cm. The measurements were performed at a frequency of 172 Hz and a sinusoidal current excitation, $I_o \sin(\omega t)$, with amplitude of $I_o = 7$ mA applied using an alternating current source meter. Figure 9 shows (a) transverse Hall and (b) longitudinal resistance measured as a function of applied external field. We can see from Fig. 9(b) that the Hall resistance is dominated by planar Hall effect of the order of 0.4% as compared to very small spin Hall magnetoresistance (0.05%). We estimated the value of perpendicular anisotropy field, $\mu_0 H_k = 0.25$ T, by linear fitting of the experimental data shown in Fig. 9(a) at high fields. We were able to quantify the effective DL-SOT and FL-SOT of the Ni film by second harmonic-Hall resistance ($R_{2\omega}$) measurements. The sample was rotated to vary in-plane field orientations as shown in Fig. 9(d) for the applied external field of 0.2 T. The data points are fitted using the standard equation for the second harmonic-Hall resistance given by [53]

$$\begin{aligned} R_{2\omega} &= \frac{1}{2}\left(R_{AHE}\frac{H_{DL}}{H_k + H_{ext}} + R_{const}\right)\cos\theta \\ &\quad - \left(R_{PHE}\frac{H_{FL+Oe}}{H_{ext}}\right)\cos 2\theta \cos\theta \\ &= A\cos\theta + B\cos 2\theta\cos\theta, \end{aligned} \tag{3}$$

where θ is the angle between applied external field and current. R_{AHE}, R_{PHE}, H_k, H_{DL}, and H_{FL+Oe} are the anomalous Hall resistance, planar Hall resistance, perpendicular anisotropy field, DL spin-orbit effective field, and combined FL spin-orbit and Oersted effective field, respectively. R_{const} is the component of the $R_{2\omega}$ which is independent of the applied field. The fitted curves in Fig. 9(d) show the contribution from the $\cos\theta$ component (prefactor A: red line) and $\cos 2\theta \cos\theta$ component (prefactor B: blue line). The resultant fit (black line) is the sum of two components. The values of prefactors A and B obtained from fittings are plotted as a function of $1/(H_k + H_{ext})$ and $1/(H_{ext})$ in Figs. 9(e) and 9(f), respectively. It can be seen that as the field is increased, the FL contribution diminishes and only the DL contribution remains. The linear fits to the plots give the value of H_{DL} and H_{FL+Oe} from which we estimate the DL(FL) efficiency using Eq. (1). The value of $\xi_{DL} \approx 0.08 \pm 0.01$. The FL contribution, $\xi_{FL} \approx 0.03 \pm 0.003$, can be explained as entirely coming from Oersted field due to 1-nm-thick Pt layer. The DL and FL efficiencies are similar to values calculated from FMR measurements. The consistency of the DL and FL efficiency values obtained from both methods justify the claim that multilayer epitaxial samples show better DL and FL efficiency. A detailed discussion and possible reasoning for variation of efficiency with multilayer growth and crystallinity follow in the next section.

IV. DISCUSSION

In this section, we discuss possible sources of large DL and FL torque generation efficiencies in multilayer and epitaxial samples. Both epitaxial samples (K-01 and K-03) show larger ξ_{DL} than the polycrystalline counterparts. While a number of parameters contribute to ξ_{DL}, we speculate a few, as follows. The momentum scattering rate is expected to be different between polycrystalline and epitaxial samples due to different numbers of, e.g., defects, crystallographic domain boundaries, and chemical disorders. This difference naturally leads to the variation of resistivity, the extrinsic SHE, as well as the spin-relaxation rate. Nguyen *et al.* [54] and Lee *et al.* [55] systematically demonstrated that the spin-transport parameters significantly vary with Pt resistivity. In addition, we would like to mention that epitaxial and polycrystalline Pt films display dissimilar relationship between the spin and momentum scattering rates, attributed to EY and DP spin-relaxation mechanisms [37]. This difference might play a

role for ξ_{DL} since ξ_{DL} is a device parameter including the spin-relaxation rate in our model. Furthermore, electrons in epitaxial films flow along the specific crystallographic orientation in our devices. The spin-orbit property of electrons populated around the corresponding momentum point in the Fermi surface determines ξ_{DL}. This is not the case for the polycrystalline samples where ξ_{DL} has contributions from all momentum points across the entire Fermi surface. Indeed, the notable difference in spin-torque generation between epitaxial and polycrystalline Co/Pt samples has been reported by Ryu *et al.* [39].

In our experiments, the magnitude of DL torque efficiency is always larger in multilayer samples than bilayers. This is unexpected because both DL and FL torques should be canceled in a Ni layer sandwiched by two Pt layers, i.e., those in our multilayers where only the bottom-most Ni layer is expected to be torqued when we apply a current. This does not seem to be the case in our devices where sizable spin torques were experimentally observed, suggesting that the spin-torque properties in our multilayer device are not as simple as the ideal case. For example, the quality of the top and bottom interfaces cannot be necessarily the same due to different magnitudes of intermixing and/or strain propagation at the interfaces [56,57]. This is supported by our x-ray reflectivity (XRR) results presented in Appendix A, where we are required to introduce intermixing (NiPt alloy) layers to fit the experimental data well for epitaxial multilayer samples, whereas polycrystalline samples do not need such addition for better fitting. The best-fit parameters indicate that the upper and lower interfaces sandwiching the ferromagnetic layer are not equivalent in multilayer samples. The different interface quality hence suggests nonvanishing spin currents injected from the top and bottom Pt layers, exerting measurable torques in our experiments. It has been shown experimentally that DL and FL torques are modified by consequent intermixing [8] and insertion of spacer layers [58] between the ferromagnet and the nonmagnet. The upper/lower interface quality would also lead to asymmetric interfacial spin absorption that potentially contributes to the large SOT magnitude in multilayer samples. For multilayer growth, the film quality tends to be improved with growth due to lesser contributions of lattice mismatch and the roughness from the substrate as growth continues. The resultant sharp interfaces may lead to enhancement of SOTs, as shown in previous works [40,59].

Finally, we consider other current-induced spin-torque generation mechanisms [4,60,61]. It is possible to imagine self-induced torques [20,62] due to spin current flowing in the Ni layers, where the asymmetry in top and bottom interfaces can induce an additional SOT [20]. We cannot rule out the possibility of potential contributions from orbital Hall effect due to the long-range orbital current generated in Pt [21,63].

V. CONCLUSION

In this paper, we presented the measurement of DL and FL torque efficiencies in Ni/Pt multilayer and bilayer samples using techniques of SOT-FMR and harmonic Hall resistance. The effects of layer stacking and crystal orientation on SOT was examined. We found that the DL torque efficiency (ξ_{DL}) is enhanced by multilayer epitaxial growth and the value of ξ_{DL} per unit applied current density obtained for epitaxial multilayer samples (0.08 ± 0.01) ~160% larger than the value for bilayer polycrystalline samples (0.03 ± 0.002). The results show a large spin Hall angle in multilayer samples, without cancellation coming from the symmetry of stacking structure, which is attributable to the different interface qualities between upper and lower interfaces. The value of $\theta_{SHA} \sim 0.15$ in multilayer epitaxial films is larger than previous reported values. These findings provide a route for enhancement of DL SOT efficiency through multilayer epitaxial growth. The results also indicate that epitaxial samples show larger ξ_{FL} compared to the polycrystalline samples. Apart from the bulk spin Hall and interfacial effects, some other sources such as self-induced SOTs in Ni and orbital Hall effect can potentially play an important role in SOT generation. Although we could not experimentally separate the different contributions to SOTs, the relatively large efficiency of spin current generation that is observed is promising for applications that utilize SHE to manipulate ferromagnetic dynamics. Our results shed light on the importance of crystal orientation, multilayering, and interface quality for enhancing the magnitude of SOT which is important for spintronic devices.

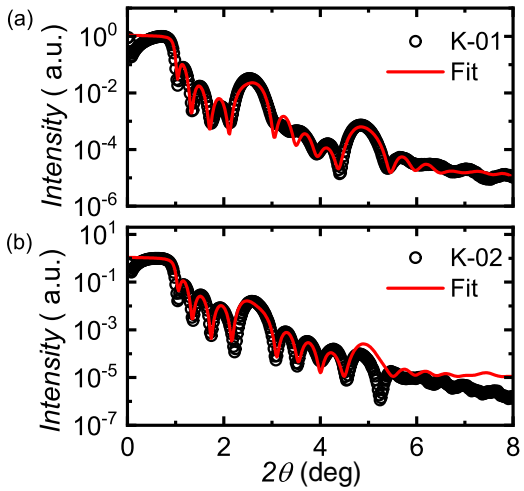

FIG. 10. X-ray reflectivity profiles for multilayer samples. Solid lines are fitting results.

ACKNOWLEDGMENTS

A.S. thanks the JSPS Postdoctoral fellowship for research in Japan (No. P21777) and EPSRC for their support through the NPIF EPSRC Doctoral studentship (No. EP/R512400/1). T.S. is supported by Grant-in-Aid for Scientific Research (A) (No. JP20H00299) and Grant-in-Aid for Scientific Research (S) (No. JP18H05246) from JSPS KAKENHI.

APPENDIX A: XRR MEASUREMENTS

To determine the thickness of the films and the surface roughness, XRR measurements were performed as shown in Fig. 10 using scintillation counter. The good quality of films is confirmed from the presence of a large number of fringes. The data points were fitted by the Globalfit software

TABLE III. Fitting parameters for x-ray reflectivity measurements.

Sample	Layer	Density (g/cm^3)	$d(nm)$ thickness	$\sigma(nm)$ roughness
	Pt	21.5 ± 0.01	1.0 ± 0.03	1.24 ± 0.03
	NiPt	11.9 ± 0.06	0.4 ± 0.02	0.17 ± 0.01
$K-01$	Ni	8.9 ± 0.01	1.9 ± 0.01	0.11 ± 0.02
	NiPt	11.5 ± 0.04	0.6 ± 0.02	0.09 ± 0.01
	Al_2O_3	1.8 ± 0.01	3.1 ± 0.01	0.18 ± 0.01
	Pt	21.5 ± 0.01	1.1 ± 0.02	1.3 ± 0.02
$K-02$	Ni	8.9 ± 0.04	2.5 ± 0.02	0.4 ± 0.01
	Al_2O_3	1.6 ± 0.03	2.8 ± 0.05	0.1 ± 0.01

of Rigaku using a multilayer structure consisting of Ni and Pt layers. The fitting parameters are summarized in Table III. The surface roughness obtained was ∼0.5 nm. For sample K-01, the existence an of intermixing layer (i.e., a very thin Ni-Pt alloy layer) is assumed to fit the experimental XRR. Without considering the intermixing layer, the experimental XRR cannot be fitted numerically. This intermixing is attributed to the substrate deposition temperature of 400 °C. This might be related to the higher DL torque for the epitaxial Ni/Pt. For the polycrystalline K-02 sample, an intermixing layer (i.e., Ni-Pt alloy layer) is not taken into account because the room temperature deposition for K-02 did not promote intermixing. Even without an intermixing layer, the experimental XRR is fairly fitted numerically.

APPENDIX B: XRD PROFILE CALCULATIONS

In the case of the metallic superlattice, the step model is applicable to explain the peak positions for the experimental XRD profile. The x-ray scattering intensity $[I(Q)]$ for the metallic superlattice consisting of Ni and Pt is given by $I(Q) = I_e|F_{\mathrm{Ni}}(Q) + F_{\mathrm{Pt}}(Q)\exp(iQD_{\mathrm{Ni}})|^2 |\sum_{k=0}^{N-1}\exp(iQk\Lambda)|^2$, where I_e is Thomson scattering intensity, $F_{\mathrm{Ni(Pt)}}(Q)$ is the structural factor of Ni(Pt), D_{Ni} is the thickness of the Ni layer, Λ is the superlattice period, and Q is the scattering vector. $|\sum_{k=0}^{N-1}\exp(iQk\Lambda)|^2$ corresponds to the Laue function $L(Q)$ and is expressed as $L(Q) = |\sum_{k=0}^{N-1}\exp(iQk\Lambda)|^2 = \frac{\sin^2(\frac{NQ\Lambda}{2})}{\sin^2(\frac{Q\Lambda}{2})}$, where N is the repetition number. The term of the structural factor is expressed as

$$
\begin{aligned}
&|F_{\mathrm{Ni}}(Q) + F_{\mathrm{Pt}}(Q)\exp(iQD_A)|^2 \\
&\quad = |F_{\mathrm{Ni}}(Q)|^2 + |F_{\mathrm{Pt}}(Q)|^2 + F_{\mathrm{Ni}}(Q)F_{\mathrm{Pt}}{}^*(Q)\exp(-iQD_{\mathrm{Ni}}) \\
&\qquad + F_{\mathrm{Ni}}{}^*(Q)F_{\mathrm{Pt}}(Q)\exp(iQD_{\mathrm{Ni}i}).
\end{aligned}
$$

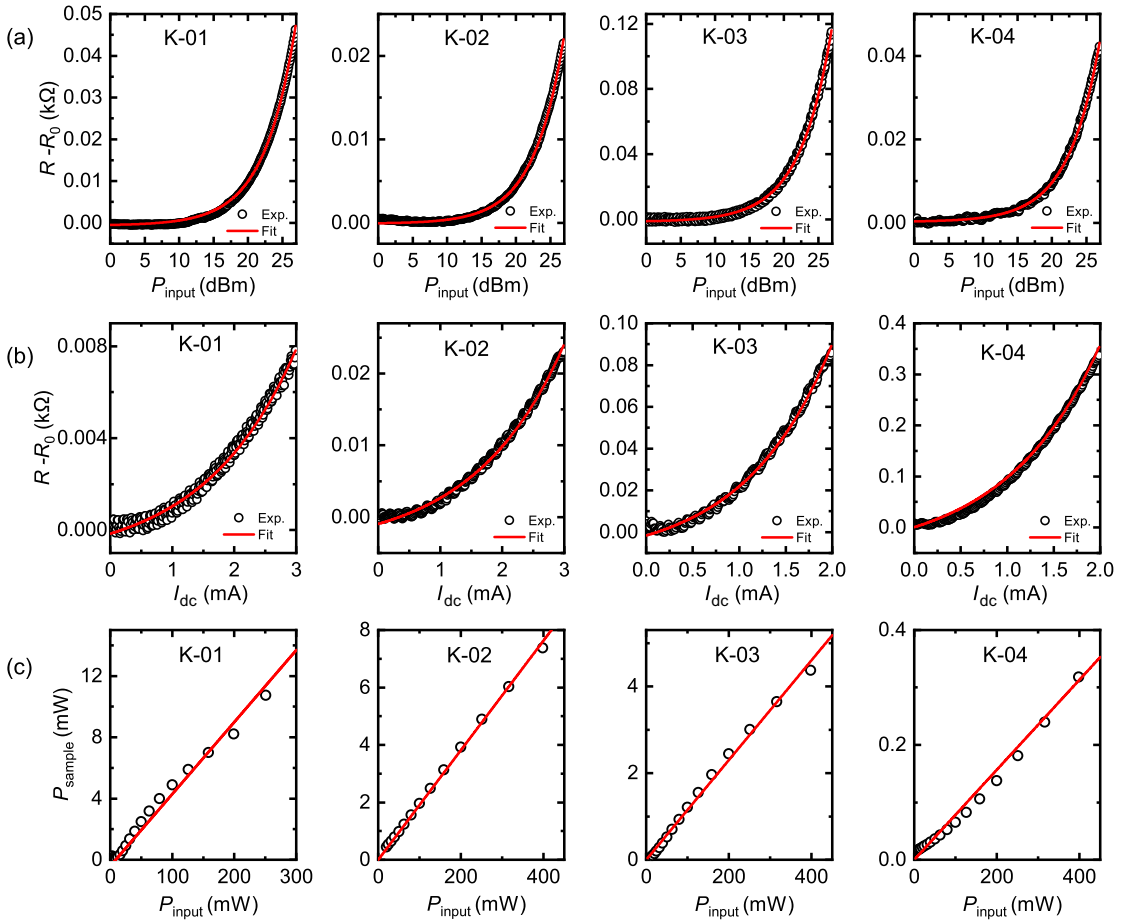

FIG. 11. (a) Resistance change as a function of microwave power for four sets of samples. (b) Resistance change as a function of dc current and (c) power from source as a function of the power in the sample for different samples.

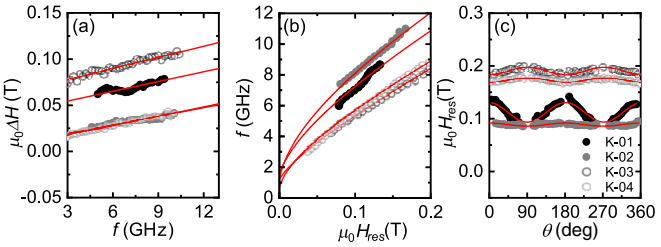

FIG. 12. (a) Frequency dependence of the half width at half maximum (HWHM) linewidth at $\theta = 45^\circ$ for allsamples. The inhomogeneous broadening is obtained from the intercept by fitting the data with linear fit and the slope gives the Gilbert damping component, α. (b) Resonance field, $\mu_0 H_{\rm res}$ as a function of frequency at an angle $\theta = 45^\circ$ for all samples. The solid lines are the fittings. (c) In-plane angular dependence of resonance field $\mu_0 H_{\rm res}$ obtained from fitting the FMR scans for different set of samples measured at 8 GHz.

Using the areal atomic density ($\eta_{\rm Ni}$ and $\eta_{\rm Pt}$), lattice spacing ($d_{\rm Ni}$ and $d_{\rm Pt}$), atomic scattering factor($f_{\rm Ni}$ and $f_{\rm Pt}$), and number of lattice planes ($n_{\rm Ni}$ and $n_{\rm Pt}$), the term of the structural factor can be transformed into

$$|F(Q)|^2 = f_{\rm Ni}^2(Q)\eta_{\rm Ni}^2 \frac{\sin^2\left(\frac{n_{\rm Ni}Qd_{\rm Ni}}{2}\right)}{\sin^2\left(\frac{Qd_{\rm Ni}}{2}\right)} + f_{\rm Pt}^2(Q)\eta_{\rm Pt}^2 \frac{\sin^2\left(\frac{n_{\rm Pt}Qd_{\rm Pt}}{2}\right)}{\sin^2\left(\frac{Qd_{\rm Pt}}{2}\right)} + 2f_{\rm Ni}(Q)f_{\rm Pt}(Q)\eta_{\rm Ni}\eta_{\rm Pt} \frac{\sin\left(\frac{n_{\rm Ni}Qd_{\rm Ni}}{2}\right)}{\sin\left(\frac{Qd_{\rm Ni}}{2}\right)} \frac{\sin\left(\frac{n_{\rm Pt}Qd_{\rm Pt}}{2}\right)}{\sin\left(\frac{Qd_{\rm Pt}}{2}\right)} \times \cos\left(\frac{\Lambda Q}{2}\right).$$

Then, the x-ray scattering intensity was calculated for $[{\rm Ni}(3\,{\rm nm})/{\rm Pt}(1\,{\rm nm})]_{\rm x5}$ with the (111) crystal orientation.

APPENDIX C: MICROWAVE CALIBRATION

There is a large impedance mismatch between microwave lines and the sample (with a few thousand Ω in resistance) which causes a large amount of power reflection from the devices. As a result, the amount of power reaching the sample is a fraction of power supplied from the source. To quantify the actual power reaching the device, we used a bolometric technique [4,64] in which we compared the resistance change caused due to joule heating when a known dc current, $I_{\rm dc}$, flows in the sample with that caused by the flow of microwave power, $P_{\rm input}$. Figure 11 shows the resistance change by two excitations. The current flowing through the device ($I_{\rm dc}$) is quantified at a given microwave frequency and then the microwave power at sample is calculated by scaling it with

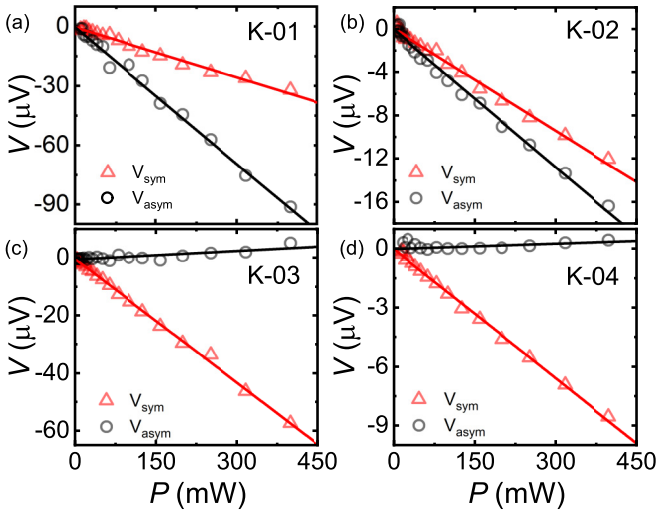

FIG. 13. Plot of magnitude of the voltage for the symmetric and antisymmetric components as a function of injected microwave powers for different set of samples at $f = 8$ GHz for K-01 and K-02 and 6 GHz for K-03, K-04. All the samples show linear dependence for the given regime of injected power.

sample resistance. Figure 11(c) shows the microwave power at the sample plotted against input microwave power ($P_{\rm input}$). It can be seen that that power input at the sample is fraction of the power from the microwave source. For samples K-03 and K-04, which had higher resistance, the current reaching the sample is smaller as compared to K-01 and K-02.

APPENDIX D: FITTING EQUATION FOR FMR DATA

The expression for dc signal from spin rectification used for fitting the FMR data is given as

$$V_{\rm dc} = V_{\rm sym}\frac{\Delta H^2}{(H_{\rm ext}-H_{\rm res})^2+\Delta H^2} + V_{\rm asym}\frac{(H_{\rm ext}-H_{\rm res})\Delta H}{(H_{\rm ext}-H_{\rm res})^2+\Delta H^2}, \quad \text{(D1)}$$

where $V_{\rm sym}$ and $V_{\rm asym}$ are the Lorentzian components in symmetric and antisymmetric line shape given below:

$$V_{\rm sym} = \frac{I_0\Delta R}{2}\frac{\omega}{\mu_0\gamma\Delta H(2H_{\rm res}+H_1+H_2)}h_z\sin 2\theta = \frac{I_0\Delta R}{2}A_{\rm sym}h_z\sin 2\theta, \quad \text{(D2)}$$

TABLE IV. Summary of the anisotropy constants and magnetization obtained from fitting of frequency-dependent resonance field and linewidth data. Note: The uncertainty values reported here are the standard error of the fitting parameters obtained from curve fitting.

Sample	$\mu_0 H_{2\parallel}$(mT)	$\mu_0 H_{2\perp}$(T)	$\mu_0 M_{\rm eff}$(T)	$\mu_0 M_s$(T)	α	$\mu_0\Delta H_0$(T)
K-01	5.62 ± 0.1	-0.24 ± 0.006	0.60 ± 0.06	0.362 ± 0.05	0.11 ± 0.01	0.0439 ± 0.0005
K-02	3.15 ± 0.01	-0.38 ± 0.005	0.71 ± 0.05	0.331 ± 0.05	0.093 ± 0.005	0.0092 ± 0.0004
K-03	-8.15 ± 0.2	0.15 ± 0.004	0.23 ± 0.03	0.377 ± 0.02	0.115 ± 0.005	0.065 ± 0.001
K-04	-2.15 ± 0.04	-0.02 ± 0.004	0.32 ± 0.04	0.298 ± 0.04	0.096 ± 0.003	0.0093 ± 0.0007

TABLE V. Summary of the anisotropy constants and magnetization obtained from fitting of angular dependence of resonance field. Note: The uncertainty values reported here are the standard error of the fitting parameters obtained from curve fitting.

Sample	$\mu_0 H_{2\parallel}$(mT)	$\mu_0 H_{2\perp}$(T)	$\mu_0 M_{\text{eff}}$(T)	$\mu_0 M_s$(T)
K-01	19.1 ± 0.1	-0.35 ± 0.01	0.712 ± 0.06	0.362 ± 0.05
K-02	3.01 ± 0.01	-0.43 ± 0.01	0.761 ± 0.05	0.331 ± 0.05
K-03	-8.1 ± 0.1	0.142 ± 0.002	0.235 ± 0.02	0.377 ± 0.02
K-04	-4.2 ± 0.1	-0.011 ± 0.004	0.309 ± 0.04	0.298 ± 0.04

$$V_{\text{asym}} = \frac{I_0 \Delta R}{2} \frac{(H_{\text{res}} + H_1)}{\Delta H(2H_{\text{res}} + H_1 + H_2)} \times (-h_x \sin\theta + h_y \cos\theta) \sin 2\theta = \frac{I_0 \Delta R}{2} A_{\text{asy}}(-h_x \sin\theta + h_y \cos\theta). \quad \text{(D3)}$$

The terms A_{sym} and A_{asy} are the scalar amplitudes of the magnetic susceptibility ($A_i = \chi_i/M_s$) and depend on the magnetic anisotropy of the device. The other terms are the external field (H_{ext}) and H_1, H_2 are the terms containing the demagnetization field and in-plane/out-of-plane anisotropy fields. h_x, h_y, h_z are components of the current-induced effective field at microwave frequency, f, which drives the magnetic moments given as $\mathbf{h}_{\text{eff}} = (h_x, h_y, h_z)e^{j2\pi ft}$. γ, M_s, H_{res}, ΔH, I_0, and ΔR are the gyromagnetic ratio, saturation magnetization, resonance field, half width at half maximum linewidth of resonance, current amplitude in the device, and AMR resistance change respectively.

The anisotropy fields used for obtaining H_1, H_2 are calculated by fitting the frequency dependence of the resonance field shown in Fig. 12(b) using Kittel resonance formula [65]. The in-plane uniaxial ($\mu_0 H_{2\parallel}$) and perpendicular anisotropy ($\mu_0 H_{2\perp}$) fields obtained from fitting are summarized in Table IV. Also, the values of effective saturation magnetization field ($M_{\text{eff}} = M_s - H_{2\perp}$) are given in Table IV. It can be seen that the uniaxial anisotropy component is dominant in comparison to biaxial for all samples. The polycrystalline samples show very little anisotropy compared to epitaxially grown samples. There can be a contribution from strain-induced anisotropy in epitaxially grown samples [66]. The multilayer samples exhibit a large perpendicular anisotropy field ($\mu_0 H_{2\perp}$) which can be explained by the scenario that the multilayering improves the magnitude of crystal orientation and the resultant sharp interface may lead to the increase in the strain effect. As another check, we also estimated the value of anisotropy fields by fitting the angular dependence of the resonance field using the Kittel resonance formula [67] as shown in Fig. 12(c), and the values are summarized in Table V in Appendix. The values match fairly well with those calculated from frequency dependence. We obtained the values of the inhomogeneous broadening $\mu_0 \Delta H_0$ and intrinsic gilbert damping α for our films by fitting the frequency dependence of linewidth $\mu_0 \Delta H$ using Eq. (D4) (the values obtained from fitting are summarized in Table IV):

$$\mu_0 \Delta H = \mu_0 \Delta H_0 + \frac{2\pi\alpha}{\gamma} f. \quad \text{(D4)}$$

The value of α is fairly constant and very large $\sim$0.1 for all samples, as can be seen in Table IV. Similar damping values amongst all the samples suggest that damping is not affected by crystal structure. The enhancement of α in the measured films can originate from several mechanisms and one such mechanism can be due to spin pumping [68]. To quantify the spin pumping term, a detailed analysis is required which is beyond the scope of this paper. Nevertheless, from Fig. 12(a) it can be seen that the inhomogeneous contribution for samples grown on sapphire is larger than that grown on SiO_2 substrate, which can be due to strain induced magnetic inhomogeneity. Strain can be induced by growth [69] due to the lattice mismatch [66]. In our films, there is a lattice mismatch between Pt (lattice constant $a = 3.93$ Å) grown on sapphire (lattice constant $a = 4.75$ Å [70]), which can cause strain induced anisotropy [66].

APPENDIX E: POWER DEPENDENCE OF RECTIFIED VOLTAGE

From Eqs. (D2) and (D3), it is found that $V_{\text{sym}}, V_{\text{asy}} \propto I^2$, where h_i, $(i = x, y, z) \propto I$. This can be seen from the linear

TABLE VI. SOT effective fields for different samples measured at $f = 8$ GHz. All of them have been scaled by a current density of $j = 10^{10} A/m^2$.

Parameter	Sample K-01	K-02	K-03	K-04
$\mu_0 h_y$ (mT)	-0.14 ± 0.004	-0.08 ± 0.007	$(1.4 \pm 0.1) \times 10^{-2}$	$(2.7 \pm 0.5) \times 10^{-3}$
$\mu_0 h_x$ (mT)	$(-6.1 \pm 0.2) \times 10^{-3}$	$(-5.2 \pm 0.4) \times 10^{-5}$	$(-5.4 \pm 0.1) \times 10^{-4}$	$(-2.5 \pm 0.5) \times 10^{-4}$
μ_0a (mT)	$(2.2 \pm 0.1) \times 10^{-3}$	$(-3.2 \pm 0.2) \times 10^{-3}$	$(2.4 \pm 0.2) \times 10^{-3}$	$(5.6 \pm 0.1) \times 10^{-3}$
μ_0b (mT)	-0.29 ± 0.002	-0.245 ± 0.003	-0.163 ± 0.002	-0.121 ± 0.002
μ_0c (mT)	$(-9.02 \pm 0.1) \times 10^{-3}$	$(-6.9 \pm 0.3) \times 10^{-3}$	$(8.3 \pm 0.3) \times 10^{-3}$	$(2.7 \pm 0.2) \times 10^{-3}$
I_0 (mA)	3.2 ± 0.01	1.7 ± 0.01	1.37 ± 0.003	0.429 ± 0.001
$\Delta R(\Omega)$	4.694 ± 0.001	4.821 ± 0.001	10.751 ± 0.002	11.062 ± 0.002

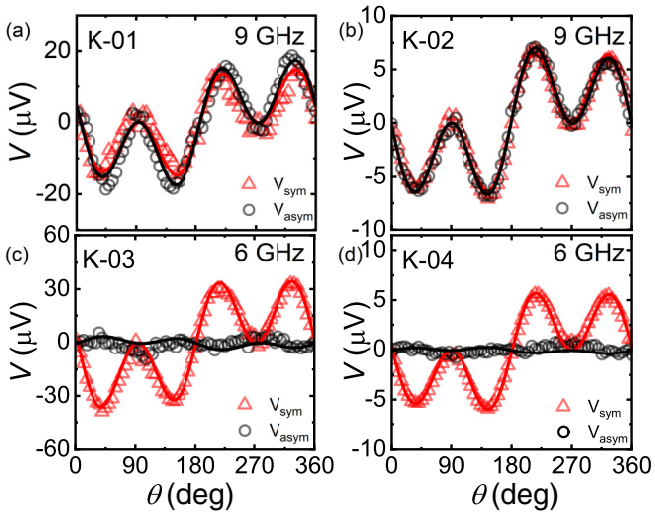

FIG. 14. The symmetric and antisymmetric components of the SOT-FMR spectra as a function of in-plane magnetic field angle θ for (a) K-01, (b) K-02, (c) K-03, and (d) K-04 films at different frequencies. The bilayer samples show negligible antisymmetric components while the antisymmetric component is comparable to the symmetric component for the multilayer samples.

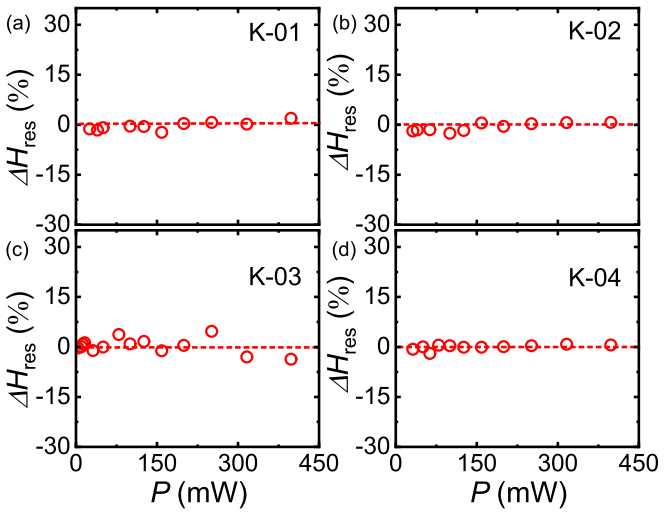

FIG. 15. Plot of change in ratio of FMR field [$\Delta H_{\rm res} = (H_{\rm res}(P) - H_{\rm avg\ res})/H_{\rm avg\ res}$] as a function of injected microwave powers for different set of samples at $f = 8$ GHz for K-01 and K-02 and 6 GHz for K-03, K-04. All the samples show zero deviation, indicating that $H_{\rm FMR}$ is independent of applied microwave power, thus indicating that for the given regime of input power, sample heating from power absorption does not affect the magnetic properties.

dependence of rectified voltage V on microwave power as shown in Fig. 13, which is consistent with our model. Also in our experiments, the wavelength of applied microwaves in the frequency range 3–12 GHz was much larger than the length of device (few hundreds of μm). This ensures that current flow is uniform and the phase is almost constant [71].

APPENDIX F: ADDITIONAL SOT-FMR RESULTS IN THIS PAPER

In addition to the results presented in the main text, we also investigated the angular dependence of the voltage at different frequencies as shown in Fig. 14. The θ dependence for samples K-01 and K-02 as shown in Figs. 14(a) and 14(b) were performed at frequency $f = 9$ GHz while for K-3 and K-04 in the bottom panel shows angular dependence performed at $f = 6$ GHz. It can be seen that for all samples, a similar angular dependence as in Fig. 5 was seen regardless of the excitation frequency.

APPENDIX G: CALCULATION OF SPIN HALL CONDUCTIVITY

The value of spin Hall conductivity ($\sigma_{\rm SH}$) is given by the equation as below:

$$\sigma_{\rm SH} = \frac{\hbar}{2e}\frac{\theta_{\rm SHA}}{(1+\theta_{\rm SHA}^2)\rho_{\rm xx}}, \tag{G1}$$

where $\rho_{\rm xx}$ is the longitudinal resistivity of Pt layer. Using Eq. (G1) and the values of $\theta_{\rm SHA}$, the value of $\sigma_{\rm SH}$ was calculated and summarized in Table II.

APPENDIX H: POWER DEPENDENCE OF RESONANCE FIELD

To quantify the effect of sample heating on magnetic properties, we plotted the change in resonance field, $\Delta H_{\rm res}$, in Fig. 15. It can be seen that there is no change in resonance field for the given regime of injected input microwave power. This shows that sample magnetic properties are not affected due to heating.

[1] L. Liu, T. Moriyama, D. C. Ralph, and R. A. Buhrman, Phys. Rev. Lett. **106**, 036601 (2011).

[2] A. Manchon, J. Železný, I. M. Miron, T. Jungwirth, J. Sinova, A. Thiaville, K. Garello, and P. Gambardella, Rev. Mod. Phys. **91**, 035004 (2019).

[3] I. M. Miron, K. Garello, G. Gaudin, P. Zermatten, M. V. Costache, S. Auffret, S. Bandiera, B. Rodmacq, A. Schuhl, and P. Gambardella, Nature (London) **476**, 189 (2011).

[4] H. Kurebayashi, J. Sinova, D. Fang, A. C. Irvine, T. D. Skinner, J. Wunderlich, V. Novák, R. P. Campion, B. L. Gallagher, E. K. Vehstedt *et al.*, Nat. Nanotechnol. **9**, 211 (2014).

[5] H. Nakayama, Y. Kanno, H. An, T. Tashiro, S. Haku, A. Nomura, and K. Ando, Phys. Rev. Lett. **117**, 116602 (2016).

[6] A. Brataas, A. D. Kent, and H. Ohno, Nat. Mater. **11**, 372 (2012).

[7] M. Hayashi, J. Kim, M. Yamanouchi, and H. Ohno, Phys. Rev. B **89**, 144425 (2014).

[8] K. Garello, I. M. Miron, C. O. Avci, F. Freimuth, Y. Mokrousov, S. Blügel, S. Auffret, O. Boulle, G. Gaudin, and P. Gambardella, Nat. Nanotechnol. **8**, 587 (2013).

[9] J. E. Hirsch, Phys. Rev. Lett. **83**, 1834 (1999).

[10] J. Sinova, D. Culcer, Q. Niu, N. A. Sinitsyn, T. Jungwirth, and A. H. MacDonald, Phys. Rev. Lett. **92**, 126603 (2004).
[11] Y. K. Kato, R. C. Myers, A. C. Gossard, and D. D. Awschalom, Science **306**, 1910 (2004).
[12] Y. A. Bychkov and E. I. Rashba, J. Phys. C **17**, 6039 (1984).
[13] V. M. Edelstein, Solid State Commun. **73**, 233 (1990).
[14] J. C. Rojas Sánchez, L. Vila, G. Desfonds, S. Gambarelli, J. P. Attané, J. M. De Teresa, C. Magén, and A. Fert, Nat. Commun. **4**, 2944 (2013).
[15] M. B. Jungfleisch, W. Zhang, J. Sklenar, W. Jiang, J. E. Pearson, J. B. Ketterson, and A. Hoffmann, Phys. Rev. B **93**, 224419 (2016).
[16] P. M. Haney, H.-W. Lee, K.-J. Lee, A. Manchon, and M. D. Stiles, Phys. Rev. B **87**, 174411 (2013).
[17] K.-W. Kim, S.-M. Seo, J. Ryu, K.-J. Lee, and H.-W. Lee, Phys. Rev. B **85**, 180404(R) (2012).
[18] C. Abert, H. Sepehri-Amin, F. Bruckner, C. Vogler, M. Hayashi, and D. Suess, Phys. Rev. Appl. **7**, 054007 (2017).
[19] S. Dutta, A. Bose, A. A. Tulapurkar, R. A. Buhrman, and D. C. Ralph, Phys. Rev. B **103**, 184416 (2021).
[20] W. Wang, T. Wang, V. P. Amin, Y. Wang, A. Radhakrishnan, A. Davidson, S. R. Allen, T. J. Silva, H. Ohldag, D. Balzar *et al.*, Nat. Nanotechnol. **14**, 819 (2019).
[21] H. Hayashi, D. Jo, D. Go, T. Gao, S. Haku, Y. Mokrousov, H.-W. Lee, and K. Ando, Commun. Phys. **6**, 32 (2023).
[22] J. Zhou, X. Wang, Y. Liu, J. Yu, H. Fu, L. Liu, S. Chen, J. Deng, W. Lin, X. Shu *et al.*, Sci. Adv. **5**, eaau6696 (2019).
[23] E. C. Ahn, npj 2D Mater. Appl. **4**, 17 (2020).
[24] G.-M. Choi, J. H. Oh, D.-K. Lee, S.-W. Lee, K. W. Kim, M. Lim, B.-C. Min, K.-J. Lee, and H.-W. Lee, Nat. Commun. **11**, 1482 (2020).
[25] J. Han and L. Liu, APL Mater. **9**, 060901 (2021).
[26] H. Hayashi, A. Musha, H. Sakimura, and K. Ando, Phys. Rev. Res. **3**, 013042 (2021).
[27] T. Nan, S. Emori, C. T. Boone, X. Wang, T. M. Oxholm, J. G. Jones, B. M. Howe, G. J. Brown, and N. X. Sun, Phys. Rev. B **91**, 214416 (2015).
[28] H.-Y. Lee, S. Kim, J.-Y. Park, Y.-W. Oh, S.-Y. Park, W. Ham, Y. Kotani, T. Nakamura, M. Suzuki, T. Ono *et al.*, APL Mater. **7**, 031110 (2019).
[29] H. An, Y. Kanno, A. Asami, and K. Ando, Phys. Rev. B **98**, 014401 (2018).
[30] A. J. Berger, E. R. J. Edwards, H. T. Nembach, O. Karis, M. Weiler, and T. J. Silva, Phys. Rev. B **98**, 024402 (2018).
[31] C.-F. Pai, Y. Ou, L. H. Vilela-Leão, D. C. Ralph, and R. A. Buhrman, Phys. Rev. B **92**, 064426 (2015).
[32] W. Zhang, W. Han, X. Jiang, S.-H. Yang, and S. SP Parkin, Nat. Phys. **11**, 496 (2015).
[33] N. H. Long, P. Mavropoulos, D. S. G. Bauer, B. Zimmermann, Y. Mokrousov, and S. Blügel, Phys. Rev. B **94**, 180406(R) (2016).
[34] R. Freeman, A. Zholud, Z. Dun, H. Zhou, and S. Urazhdin, Phys. Rev. Lett. **120**, 067204 (2018).
[35] R. J. Elliott, Phys. Rev. **96**, 266 (1954).
[36] Y. Yafet, Phys. Rev. **85**, 478 (1952).
[37] J. Ryu, M. Kohda, and J. Nitta, Phys. Rev. Lett. **116**, 256802 (2016).
[38] S. Woo, M. Mann, A. J. Tan, L. Caretta, and G. S. Beach, Appl. Phys. Lett. **105**, 212404 (2014).
[39] J. Ryu, C. O. Avci, S. Karube, M. Kohda, G. S. Beach, and J. Nitta, Appl. Phys. Lett. **114**, 142402 (2019).
[40] G. Choi, J. Ryu, R. Thompson, J.-G. Choi, J. Jeong, S. Lee, M.-G. Kang, M. Kohda, J. Nitta, and B.-G. Park, APL Mater. **10**, 011105 (2022).
[41] A. Kumar, N. Behera, R. Gupta, S. Husain, H. Stopfel, V. Kapaklis, R. Brucas, and P. Svedlindh, J. Phys. D **53**, 355003 (2020).
[42] K.-F. Huang, D.-S. Wang, H.-H. Lin, and C.-H. Lai, Appl. Phys. Lett. **107**, 232407 (2015).
[43] Y. Wu, K. Meng, J. Miao, X. Xu, and Y. Jiang, J. Magn. Magn. Mater. **472**, 14 (2019).
[44] Y. Ishikuro, M. Kawaguchi, T. Taniguchi, and M. Hayashi, Phys. Rev. B **101**, 014404 (2020).
[45] M. Jamali, K. Narayanapillai, X. Qiu, L. M. Loong, A. Manchon, and H. Yang, Phys. Rev. Lett. **111**, 246602 (2013).
[46] T. Seki, M. Tsujikawa, K. Ito, K. Uchida, H. Kurebayashi, M. Shirai, and K. Takanashi, Phys. Rev. Mater. **4**, 064413 (2020).
[47] T. Skinner, M. Wang, A. Hindmarch, A. Rushforth, A. Irvine, D. Heiss, H. Kurebayashi, and A. Ferguson, Appl. Phys. Lett. **104**, 062401 (2014).
[48] Z. Feng, J. Hu, L. Sun, B. You, D. Wu, J. Du, W. Zhang, A. Hu, Y. Yang, D. M. Tang, B. S. Zhang, H. F. Ding, Phys. Rev. B **85**, 214423 (2012).
[49] K. Kondou, H. Sukegawa, S. Mitani, K. Tsukagoshi, and S. Kasai, Appl. Phys. Express **5**, 073002 (2012).
[50] M. Obstbaum, M. Härtinger, H. G. Bauer, T. Meier, F. Swientek, C. H. Back, and G. Woltersdorf, Phys. Rev. B **89**, 060407(R) (2014).
[51] A. Sud, Y. Koike, S. Iihama, C. Zollitsch, S. Mizukami, and H. Kurebayashi, Appl. Phys. Lett. **118**, 032403 (2021).
[52] J.-Y. Kim, D.-S. Han, M. Vafaee, S. Jaiswal, K. Lee, G. Jakob, and M. Kläui, Appl. Phys. Lett. **117**, 142403 (2020).
[53] T. Seki, Y.-C. Lau, S. Iihama, and K. Takanashi, Phys. Rev. B **104**, 094430 (2021).
[54] M.-H. Nguyen, D. C. Ralph, and R. A. Buhrman, Phys. Rev. Lett. **116**, 126601 (2016).
[55] J. W. Lee, Y.-W. Oh, S.-Y. Park, A. I. Figueroa, G. van der Laan, G. Go, K.-J. Lee, and B.-G. Park, Phys. Rev. B **96**, 064405 (2017).
[56] N.-H. Kim, J. Cho, J. Jung, D.-S. Han, Y. Yin, J.-S. Kim, H. J. Swagten, K. Lee, M.-H. Jung, and C.-Y. You, AIP Adv. **7**, 035213 (2017).
[57] D.-O. Kim, K. M. Song, Y. Choi, B.-C. Min, J.-S. Kim, J. W. Choi, and D. R. Lee, Sci. Rep. **6**, 25391 (2016).
[58] X. Fan, J. Wu, Y. Chen, M. J. Jerry, H. Zhang, and J. Q. Xiao, Nat. Commun. **4**, 1799 (2013).
[59] G. Choi, J. Ryu, S. Lee, J. Kang, N. Noh, J. M. Yuk, and B.-G. Park, Adv. Mater. Interfaces **9**, 2201317 (2022).
[60] V. P. Amin and M. D. Stiles, Phys. Rev. B **94**, 104419 (2016).
[61] V. P. Amin and M. D. Stiles, Phys. Rev. B **94**, 104420 (2016).
[62] N. Soya, M. Yamada, K. Hamaya, and K. Ando, Phys. Rev. Lett. **131**, 076702 (2023).
[63] D. Go, D. Jo, K.-W. Kim, S. Lee, M.-G. Kang, B.-G. Park, S. Blügel, H.-W. Lee, and Y. Mokrousov, Phys. Rev. Lett. **130**, 246701 (2023).
[64] D. Fang, H. Kurebayashi, J. Wunderlich, K. Výborný, L. P. Zârbo, R. Campion, A. Casiraghi, B. Gallagher, T. Jungwirth, and A. Ferguson, Nat. Nanotechnol. **6**, 413 (2011).
[65] C. Kittel, Phys. Rev. **73**, 155 (1948).

[66] A. Krysztofik, S. Özoğlu, R. D. McMichael, and E. Coy, Sci. Rep. **11**, 14011 (2021).
[67] M. Farle, Rep. Prog. Phys. **61**, 755 (1998).
[68] T. Moriyama, K. Hayashi, K. Yamada, M. Shima, Y. Ohya, Y. Tserkovnyak, and T. Ono, Phys. Rev. B **101**, 060402(R) (2020).
[69] N. Zhao, A. Sud, H. Sukegawa, S. Komori, K. Rogdakis, K. Yamanoi, J. Patchett, J. W. A. Robinson, C. Ciccarelli, and H. Kurebayashi, Phys. Rev. Mater. **5**, 014413 (2021).
[70] E. R. Dobrovinskaya, L. A. Lytvynov, and V. Pishchik, *Sapphire. Material, Manufacturing, Applications*, Micro- and Opto-Electronic Materials, Structures, and Systems (Springer, Boston, MA, 2009), pp. 55–176.
[71] Y. Li, H. Saglam, Z. Zhang, R. Bidthanapally, Y. Xiong, J. E. Pearson, V. Novosad, H. Qu, G. Srinivasan, A. Hoffmann *et al.*, Phys. Rev. Appl. **11**, 034047 (2019).